Submitted to Ap.J. - Dec. 4,2003.

A Numerical Study of the Breakout Model for CME Initiation

P. MacNeice[1]

macneice@alfven.gsfc.nasa.gov

S.K. Antiochos[2]

antiochos@nrl.navy.mil

A. Phillips[1]

phillips@sommerfeld.gsfc.nasa.gov

D.S. Spicer[3]

spicer@gauss.gsfc.nasa.gov

C.R. DeVore[2]

devore@lcp.nrl.navy.mil

and

K. Olson[4]

olson@bohr.gsfc.nasa.gov

ABSTRACT

A leading theory for the initiation of coronal mass ejections (CME) is the so-called breakout model in which magnetic reconnection above a filament channel

[1]Physics Department Drexel University, Philadelphia, PA 19104.

[2]Naval Research Laboratory, Washington, D.C. 20375.

[3]NASA, GSFC, Greenbelt, MD 20771.

[4]University of Maryland, Baltimore County, Baltimore, MD 21250.

is responsible for disrupting the coronal magnetic field. We present the first simulations of the complete breakout process including the initiation, the plasmoid formation and ejection, and the eventual relaxation of the coronal field to a more potential state. These simulations were performed using a new numerical code, which solves the numerical cavitation problems that prevented previous simulations from calculating a complete ejection. Furthermore, the position of the outer boundary in the new simulations is increased out to 30 solar radii, which enables determination of the full structure and dynamics of the ejected plasmoid. Our results show that the ejection occurs at speeds of order the coronal Alfven speed and, hence, that the breakout model can produce fast CMEs. Another key result is that the ejection speed is not sensitive to the refinement level of the grid used in the calculations, which implies that, at least for the numerical resistivity of these simulations, the speed is not sensitive to Lundquist number. We also calculate, in detail, the helicity of the system and show that the helicity is well conserved during the breakout process. Most of the helicity is ejected from the Sun with the escaping plasmoid, but a significant fraction (of order 10%) remains in the corona. The implications of these results for observation and prediction of CMEs and eruptive flares is discussed.

Subject headings: Sun: corona — Sun: coronal mass ejections (CMEs) — Sun: flares

1. Introduction

The most energetic and most dramatic manifestations of solar activity are the giant disruptions of magnetic field and plasma known as coronal CMEs/eruptive flares. A large CME can consist of $> 10^{16}$ gm of coronal plasma accelerated to > 1000km s^{-1} on a time scale of ~ 1000 s. (In this paper, we emphasize fast CMEs typical of a major CME/eruptive flare event, since these are the most important for space weather and the most difficult to explain theoretically.) The overriding problem in understanding the physics of fast CMEs is accounting for their explosive nature, a topic of intense theoretical study (e.g., Sturrock 1989; Van Ballegooijen & Martens 1989; Forbes & Isenberg 1991; Moore & Roumeliotis 1992; Low & Smith 1993; Mikić & Linker 1994; Wu et al. 1995; Wolfson & Saran 1998; Amari et al. 2000; Priest & Forbes 2000; Chen 2001). The basic energy source must be magnetic stress that comes through the photosphere, either by direct motions or by emergence of prestressed flux. However, the coronal system is driven very slowly: ~ 1km s^{-1} footpoint speeds compared to its characteristic Alfvén speed of ~ 1000km s^{-1}. Furthermore, the coronal field

is free to expand outward quasi-statically, which is the evolution usually observed and is expected from analytic theory of the ideal behavior of a force-free coronal magnetic field (Aly 1984, 1991; Sturrock 1991).

Due to these observational constraints, most of the present models postulate that CMEs represent the explosive release of magnetic energy stored in the corona, specifically, in the strongly non-potential magnetic field of a sheared neutral line, or filament channel (see recent reviews by Low 1996; Forbes 2000; Klimchuk 2001; Lin et al. 2003). Although a filament eruption may not be observed with every CME, it is well known that all major solar activity such as flares and CMEs are associated with a sheared neutral line (e.g.. Patty & Hagyard 1986; Schmieder et al. 1996). Furthermore, filament channels are the only locations in the Sun's corona where the field appears to be strongly non-potential and, hence, where large amounts of free energy can be stored. It appears highly likely, therefore, that the underlying cause of CMEs, eruptive flares, and filament ejections is the disruption of a force balance between the upward pressure of the sheared filament channel field and the downward tension of overlying coronal field that is quasi-potential.

A key point is that the upward pressure cannot increase rapidly, because the magnetic shear/twist is produced by the slow photospheric evolution (shear flows and/or flux emergence). Therefore, explosive events such as CMEs must be due fundamentally to the catastrophic removal of the downward magnetic tension of the overlying coronal field. Recent theory and simulation has focused on magnetic reconnection as the mechanism for the removal of the magnetic tension, (Low 1996; Forbes 2000; Klimchuk 2001; Lin et al. 2003). Only two reconnection models have been proposed that have successfully demonstrated explosive eruption with full-MHD numerical simulations: flux cancellation (Amari et al. 2000) and magnetic breakout (Antiochos et al. 1999). In the cancellation model, reconnection is postulated to occur at the photospheric neutral line below a filament channel, producing a twisted flux rope in the corona and eventually leading to a loss of equilibrium (Forbes 2000). In the breakout model reconnection at a null point above a filament channel leads to the removal of overlying flux and to an explosive outward expansion (Antiochos 1998; Antiochos et al. 1999). At present, neither model can be considered to have been either definitively verified or refuted by the observations. However, there have been a number of studies recently which strongly support a breakout interpretation for some well-observed CME/eruptive flare events (e.g., Aulanier et al. 2000; Sterling & Moore 2001).

It should be emphasized that both models predict a similar evolution once the eruption is well underway. The rapid upward expansion of the filament channel field causes a current sheet to form below the erupting field, resulting in strong reconnection there. This reconnection produces a highly twisted plasmoid that escapes from the corona and leaves behind

the hot X-ray, flare loops, as in the standard model (Carmichael 1964; Sturrock 1966; Hirayama 1974; Kopp & Pneuman 1976). An important issue for any model is the speed of the escaping plasmoid. In order to account for fast CMEs, the erupting plasma must be ejected from the Sun at speeds of order the Alfven velocity. But the previous numerical studies of breakout could not calculate the actual ejection itself (Antiochos et al. 1999). These studies were a critically important first step, because they showed how a multi-polar magnetic topology could contain sufficient free energy to open up the filament channel field and still be compatible with the Aly-Sturrock energy limit (Aly 1991; Sturrock 1991), but they could not verify that a fast CME would result. The problem was that once the eruption picked up significant speed, the reconnection at the rapidly moving coronal null led to numerical cavitation there (i.e., very low densities), and the simulations developed severe numerical inaccuracies.

Our goal in this paper is to calculate the complete evolution of the breakout eruption, including the formation and escape of the plasmoid. The main issues that we focus on are the speed of the eruption and the evolution of the magnetic helicity in the corona. We use the exact same 2.5D geometry and magnetic topology as in Antiochos et al. (1999), but we employ a more robust numerical code that mitigates the effects of cavitation by applying a mass diffusion at grid cells where the density exhibits too large a density drop. In addition, we extend the computational domain out to 30 solar radii so as to be able to follow the evolution of the plasmoid well after it has been ejected from the corona. A larger outer radius also helps minimize any effects from the boundary conditions there. The physical model and the code are described in detail below.

2. Description of Numerical Model

Our model follows that described in Antiochos et al. (1999) in most details, and so we limit our description of it to a summary of the essential features, and a detailed exposition of all significant modifications.

The idealized model has a complex initial field geometry, with azimuthal symmetry. It has four flux systems, as shown in the first panel of Figure 1. An inner flux system is centered on the equator. Mid-latitude flux systems are centered on latitude $\pm 45^{\circ}$, and at large radius there is an overlying dipole system. These four flux systems are bounded by two separatrix surfaces which intersect in the corona at an X-point (actually an X-line due to the axi-symmetry). A footpoint shear is applied to the inner equatorial flux system, which causes it to expand outward and push against the overlying field, deforming the X-point to a current sheet. Once the sheet becomes sufficiently thin, reconnection occurs between

the equatorial and overlying systems. This causes flux in the inner region to be transferred to the mid-latitude flux systems, which induces the remaining inner flux system to expand outward even faster. This feedback between the reconnection and outward expansion results in the explosive opening of the overlying field and escape of some of the sheared inner flux to infinity.

2.1. Equations

To model this scenario, we solve the equations of ideal MHD including gravitational acceleration :

$$\frac{\partial \rho}{\partial t} + \boldsymbol{\nabla} \cdot (\rho \boldsymbol{v}) = 0, \tag{1}$$

$$\frac{\partial}{\partial t}(\rho \boldsymbol{v}) + \boldsymbol{\nabla} \cdot (\rho \boldsymbol{v}\boldsymbol{v}) + \boldsymbol{\nabla} p = \frac{1}{4\pi}(\boldsymbol{\nabla} \times \boldsymbol{B}) \times \boldsymbol{B} - \rho \boldsymbol{g}, \tag{2}$$

$$\frac{\partial U}{\partial t} + \boldsymbol{\nabla} \cdot (U \boldsymbol{v}) + p \boldsymbol{\nabla} \cdot \boldsymbol{v} = 0, \tag{3}$$

and

$$\frac{\partial \boldsymbol{B}}{\partial t} = \boldsymbol{\nabla} \times (\boldsymbol{v} \times \boldsymbol{B}). \tag{4}$$

where ρ is mass density, $\boldsymbol{v}$ is velocity, p is gas pressure, $U = 3p/2$ is the internal energy, $\boldsymbol{B}$ is magnetic induction and $\boldsymbol{g}$ is gravitational acceleration.

2.2. Numerical Techniques

Our numerical code is a modified version of the code described by DeVore (1991). It uses a multi-dimensional Flux Corrected Transport(FCT) algorithm in spherical coordinates, and guarantees to preserve the divergence-free condition on the magnetic field to machine accuracy. The code is second order accurate in space and time for a uniformly spaced grid.

We have modified the application of the flux limiter to achieve greater consistency in its use across the set of equations. The FCT algorithm can be viewed as a combination of high and low order algorithms. The low order algorithm is the same as the high order algorithm, but has a known explicit diffusion, added to ensure that the low order solution retains positivity and monotonicity. For a given timestep, the solution for each equation is computed using the low order scheme. Anti-diffusive fluxes are then computed which remove as much of this additional diffusion as possible, under the constraint that the anti-diffusion step cannot introduce new extrema into the solution or accentuate any existing extrema. For

each equation the fraction of the anti-diffusive flux which can be applied without violating this constraint is recorded. We then take the minimum of the fractions associated with the mass and energy densities, and then apply these to limit the anti-diffusive fluxes used to complete the updated solutions for all the hydrodynamic variables.

From a numerical perspective, the most challenging aspect of this simulation has been to develop an algorithm which is robust enough to handle regions of ultra-low density. In this simulation we expect ultra-low density regions to develop. Where current sheets tear, we will have divergent flows at alfvenic speeds in an already low density plasma. We will also have the cross-section of a flux-rope with helical fieldlines expanding rapidly as it rises through an atmosphere in which the density varies approximately as r^{-5}. In any MHD code these ultra-low density regions pose problems associated with the temporal and spatial accuracy of the algorithms discretization, and with the assumptions inherent in the non-relativistic MHD description.

If the density in our numerical solution drops to unphysical ultra-low values in regions of strong magnetic field, the alfven speed can grow to be a significant fraction of the speed of light. To properly model this regime would require a kinetic description with relativistic equations. We would be forced to use such short timesteps to achieve stable and accurate solutions, that the calculation would be prohibitively expensive. Since we do not believe these high frequency modes are important in the global evolution of CMEs, we retain a non-relativistic MHD approximation. However we modify the momentum equation following an approach pioneered by Boris (1970), commonly known as the 'Boris correction'. [5] The time derivative in the momentum equation is replaced by

$$\frac{\partial}{\partial t}(\rho \boldsymbol{v}) \longrightarrow \frac{\partial}{\partial t}\boldsymbol{M} \tag{5}$$

$$\boldsymbol{M} = \rho\left(\boldsymbol{v}(1+q^2) - \boldsymbol{q}\boldsymbol{q}\cdot\boldsymbol{v})\right) \tag{6}$$

with

$$\boldsymbol{q} = \frac{\boldsymbol{B}}{\sqrt{4\pi\rho c^2}} = \frac{\boldsymbol{v}_a}{c} \tag{7}$$

where $\boldsymbol{v}_a$ is the alfven velocity. As the local alfven speed becomes significant in comparison with the speed of light, this has the effect of increasing the inertia associated with the momentum in the direction perpendicular to the local magnetic field. By choosing artificially low values of c in equation 7 we effectively dampen cross-field accelerations in regions of low mass density. In our code we chose a value of $c = 3000\text{km s}^{-1}$.

[5]The code used by Antiochos et al. (1999) employed a version of the Boris correction which had no dependence on the local field direction.

The 'Boris Correction' helps to reduce the risk of numerical cavitation. We also follow the standard practice in MHD codes, of setting the field-aligned component of the Lorentz force to zero. However in an ideal MHD code, when rapid reconnection occurs, significant fieldline curvature develops on scales close to the grid cell size. Inevitably this leads to errors due to spatial discretization. When these errors occur in regions of low density the potential for cavitation exists. In our FCT code we conjecture that this potential can be compounded by differences in the phase errors which occur in the solutions to the mass and momentum density equations. In the neighborhood of rapid reconnection strong Lorentz forces occur in close proximity to regions of divergent flow with low density. If phase errors cause excess momentum to bleed into these low density regions the result is excessively large velocities which can drive the evolution of the magnetic field in unphysical ways.

To avoid this problem we have developed a tunable method for additional limiting of the anti-diffusive fluxes in the neighborhood of very low densities. The factor by which the anti-diffusive fluxes are reduced is multiplied by the function

$$h(r, \theta, t) = 1 - h^*(r, \theta, t). \tag{8}$$

evaluated on the faces of each grid cell. When $h^* = 0$, no reduction in anti-diffusion occurs. We set h^* at cell center to be

$$h^* = \begin{cases} \min\left(1, [(3 - \frac{\rho}{\rho_{min}})\frac{2}{3}]^2\right), & \text{if } \rho < 3\rho_{min}; \\ 0 & \text{otherwise.} \end{cases} \tag{9}$$

This choice is somewhat arbitrary, and is designed to increase smoothly from 0 to 1 as ρ drops below $3\rho_{min}$ to $1.5\rho_{min}$. The value of h^* at each cell interface is then computed by averaging the value in the cells each side of the interface. In addition we apply a diffusive operator to h^* to spread its influence into the immediate neighborhood, with a diffusion coefficient which is given by $1/(8\ dt)$. Finally, at the start of each timestep we decay the existing value of h^* by 0.125 so that excess diffusion is maintained only as long as it is required.

We set the value of ρ_{min} to

$$\rho_{min} = \frac{1}{40}\rho(r, t = 0). \tag{10}$$

This approach is inelegant but effective in reducing the severity of cavitation events. It is applied to the hydrodynamic variables, but not to the magnetic field. Since the only additional diffusion which the magnetic field will experience is produced through the indirect influence of the extra mass and momentum diffusion, we expect this to be weak.

2.3. Numerical Grid

We assume azimuthal symmetry and, consequently, solve the MHD equations above in 2.5D.[6] The computational domain extends from an inner radial boundary ($1r_\odot$) at the solar surface, to the outer radial boundary at $30r_\odot$, and from the north pole, $\theta = 0$ to the south pole $\theta = \pi$. In principle the equator represents a symmetry plane in this idealized model, and we could choose to model only one hemisphere. However, we believe there is an important symmetry breaking process in this problem, associated with the development of magnetic islands on the equatorial radius (see section 3.1). This may influence the observed speed of eruption, and so we choose to model the full θ range.

The numerical grid has a static adaptive refinement superimposed upon a base grid that is uniformly spaced in the theta direction. The grid spacing is proportional to r in the radial direction, so that the grid cell aspect ratios are constant, and not a function of r. The base grid has a resolution of 128×256. In the inner regions we have two additional refinement levels as shown in Figure 2. Each refinement level has grid spacing reduced by a factor of 2 over the previous refinement level, so that near the equator on the inner radial boundary the resolution is equivalent to a grid of 512×1024. The figures in this paper show results from runs with this grid, but for comparison, we have also performed simulations with larger and smaller refinement levels.

The non-uniform radial spacing makes the code nominally first order accurate spatially. However, the second order error term introduced by the nonuniform spacing has a coefficient whose magnitude is determined by the rate at which the grid spacing changes. In our grids this spacing changes slowly. As a result we believe that the contribution of this error term to the total error is not larger than the contribution from the third order error terms, for the resolution we have used. We have validated the code by substituting a computationally expensive fourth order spatial interpolation function where appropriate, to make the code formally third order accurate, and have shown that this makes no significant qualitative difference to our results, at the resolution of our current grid.

2.4. Initial Conditions

The initial magnetic field is potential and consists of a combination of dipole and octupole components. Due to the azimuthal symmetry, it is easily expressed in terms of Euler

[6]The variables $\rho, \boldsymbol{v}, U, \boldsymbol{B}$ are functions of r and θ, but not ϕ since $\partial/\partial\phi = 0$, but the vectors $\boldsymbol{v}, \boldsymbol{B}$ can have non-zero components in the ϕ direction.

potentials,

$$\boldsymbol{B} = \boldsymbol{\nabla}\alpha(r,\theta)\times\boldsymbol{\nabla}\phi, \tag{11}$$

where we choose,

$$\alpha(r,\theta) = \sin^2\theta\frac{r_\odot}{r} + (3+5\cos 2\theta)\sin^2\theta\frac{r_\odot^3}{2r^3}. \tag{12}$$

This form for the flux function α produces a field with four distinct flux systems as shown in Figure 1. At large radius the field is dominated by the dipole component. Near the solar surface there is an inner flux system centered on the equator, bounded at higher and lower latitudes by two additional flux systems. There is a null point at a radius of $r = \sqrt{3}r_\odot$, and the field-lines passing through this point define separatrices bounding the four flux systems.

Since the initial numerical magnetic field only samples the analytic potential solution, the numerical Lorentz force will be approximately zero, but not exactly zero. Therefore, we subtract this small numerical Lorentz force associated with our initial field from the time-dependent Lorentz force evaluated during the simulation. As a result the initial field is a true equilibrium of our modified algorithm, and does not evolve until we perturb it.

The initial mass density is computed as a solution to the equation of hydrostatic equilibrium, with a temperature profile given by

$$T(r) = 2\times 10^6\ \frac{r_\odot}{r}\ \mathrm{K}, \tag{13}$$

and an electron number density of $2\times 10^8\mathrm{cm}^{-3}$ at the inner radial boundary.[7]. The temperature and density profiles are chosen so that the plasma beta in the model is small, in agreement with the real corona. For the form of α given above, we find that, at the solar surface, the magnetic field strength is 2G at the equator and 10G at the poles, which yields a value for beta varying from 0.5 to 0.02 at the poles. The value for beta along a radial line at the equator and at 45° are shown in Figure 3. Of course the beta diverges at the magnetic null, but we note that along the mid-latitude line, beta remains smaller than unity out to large radius.

2.5. Boundary Conditions

At the inner radial boundary ($r_\odot$), we enforce a line-tied condition on the magnetic field. This boundary is also assumed to be impenetrable. More precisely, these conditions

[7]This density is twice the base density used by Antiochos et al. (1999)

are imposed by setting

$$\frac{\partial B_r}{\partial t} = 0 \tag{14}$$

$$v_r = 0 \tag{15}$$

on the boundary.

The system is driven by imposing a shear velocity profile in the ϕ direction on the inner boundary. The shear is applied in a narrow region centered about the equatorial neutral line. The velocity is antisymmetric about the equator with a latitudinal dependence given by,

$$v_\phi = \begin{cases} 0 & \text{if } |\psi| > \Theta. \\ V_0(\psi^2 - \Theta^2)^2 \sin\psi & \text{if } |\psi| \leq \Theta. \end{cases}$$

where $\psi = (\pi/2 - \theta)$, $\Theta = \pi/15$ defines the latitudinal extent of the shear region on each side of the equator, and the shearing amplitude $V_0 = 8682.52 r_\odot(\pi/2)$. The shearing is applied with a sinusoidal time profile of period 2τ, and is imposed for a half cycle of the sinusoid, i.e. for a time interval of $\tau = 100000$s. As a consequence of this shear, the maximum angular displacement in azimuth of a field line footpoint at the photospheric boundary is $\pi/2$, which implies a maximum velocity $< 10\text{km s}^{-1}$ and an average shear velocity considerably less. From Figure 3 we note that in our model corona the Alfven speed can exceed 300km s^{-1}, which indicates that although our system is not driven as slowly as the real corona, it is still driven quasi-statically. It should be emphasized that the photospheric shear assumed in our model is merely a convenient method for driving the system, it is not meant to represent the process by which a real filament channel forms. Flux emergence is likely to play a major role in the formation process, but modeling flux emergence in a coronal simulation is very difficult computationally. As long as the system is driven quasi-statically, we do not expect the detailed process by which the shear forms to have a significant effect on the eruption dynamics, at least, in the breakout model.

In these simulations we attempted to place the outer radial boundary as far as computationally possible, $r = 30 r_\odot$, so that it would have a negligible effect on the eruption structure and evolution. As will be seen below, the eruption is well into its decay phase before the ejected plasmoid reaches the outer boundary. Open boundary conditions are imposed there. At the polar boundaries, the boundary conditions are determined from the azimuthal symmetry constraint.

3. Results

3.1. Evolution of Velocity and Energy

The evolution confirms and extends the initial results obtained by Antiochos et al. (1999). The field and plasma evolution is illustrated in a sequence of snapshots shown in Figures 1, 4, 5 and 6. Figures 4 through 6 show the evolution of the field superimposed upon color density maps of the mass density, radial velocity and helicity respectively. Note that the field-lines in our model are three dimensional objects, since we solve for all three components of $\boldsymbol{B}$. To display them here we project them onto a single plane, by plotting every point along each 3D field-line, not at its true location (r, θ, ϕ), but instead at $(r, \theta, 0)$. The field-lines in these figures have been drawn by choosing a set of starting points in the $\phi = 0$ plane and tracing the field-lines (in both positive and negative directions) beginning at each of those points. We selected starting points on the inner boundary, and at points along the equatorial radial axis. Some field-lines are terminated prematurely if they extend beyond the range $-\pi/4 < \phi < \pi/4$, or after they have accumulated 3000 arc segments, to avoid clutter. When comparing the frames at different times, it should be kept in mind that only those field lines that are traced from starting points on the inner boundary are the "same" in the different frames and, therefore, show the motion of a particular field line (assuming the evolution is ideal). In order to show the plasmoid with disconnected field lines that forms, we also use starting points along the equatorial radius. Since these points are fixed in space, the field lines traced from these points are not the same in the different frames, but they can be used to illustrated the general position of the plasmoid.

It is evident from Figure 1 that as the inner flux system is stressed, it expands outward, pushing up against the overlying field which inhibits its expansion. The X-point between the two systems deforms into a current sheet elongated in the θ direction. When the thickness of this current sheet reaches the grid scale, the effects of numerical diffusion become significant and the two systems begin to reconnect. We will refer to this reconnection as the 'breakout' reconnection. Field-lines at the outer edges of the inner flux system reconnect with overlying field, and subsequently snap back to join the inner mid-latitude flux systems, allowing the remaining inner flux system to expand further outward. As a result of the large outward expansion, the field lines deep in the inner system begin to approach an open geometry and, hence, a radial current sheet develops there. Again, when the current sheet thickness becomes of order the grid scale, diffusion becomes significant and reconnection sets in. We will refer to this as the 'flare' reconnection. The flare reconnection produces a disconnected flux rope (plasmoid) between the inner and outer flux systems, which continues to rise. The plasmoid eventually escapes from the system, and the inner field relaxes back to a configuration which is similar in general features to its original configuration, but with much less shear. We

emphasize that the flare reconnection and the production of a disconnected flux rope are certainly not unique to the breakout model. They are an inevitable consequence of eruption, and are well-known features of essentially every 2.5D model (e.g., Mikić & Linker 1994).

Another feature that is evident in 1, especially in the late stages of the eruption, is the appearance of a large magnetic island in front of the ejected plasmoid. The origin of this island is the artificial symmetry in the simulation. When the breakout current sheet becomes sufficiently extended in the θ direction so that its length to width ratio begins to exceed a factor of 10 or so, magnetic tearing occurs, causing the sheet to break up into multiple islands (Furth et al 1963). Island formation is a ubiquitous feature of 2.5D reconnection, especially in simulations with high spatial resolution so that long current sheet can develop (e.g., Karpen et al 1996). Note that in our simulation, magnetic islands also form in the flare current sheet along the radial direction. But these islands are short-lived and remain small, because they rapidly migrate either up or down along the radial current sheet and merge with the inner or outer flux systems. We expect that, in reality, islands forming in the breakout current sheet would also be short-lived, but the mathematical problem that we solve has a symmetry plane at the equator, with $\rho, p, U, v_r, B_\theta, B_\phi$ symmetric and v_ϕ, B_r anti-symmetric with respect to reflection in the equatorial plane. If an island forms that is centered about the equator, as is almost certain to occur, then due to the equatorial symmetry, such an island cannot move either up or down along the current sheet and disappear. An equatorially symmetric island can only grow indefinitely. Note that such an island chokes off the breakout reconnection by converting the X-point to an O-point. All the mass and field accumulated in the island must be ejected outward along with the plasmoid; hence, the island slows down the eruption. By simulating the full θ range rather than only a single hemisphere, as discussed in 2.3, we break the symmetry numerically, and mitigate these effects. Islands form almost immediately in the breakout current sheet, but early in the eruption they are small and there is enough numerical asymmetry present to move them up or down. It is only in the late stages when the ejection is moving near the Alfven speed that a large persistent island forms.

The critical issue for any CME model is the speed of the eruption. To account for fast CMEs, the ejection speed must be of order the Alfven velocity. Furthermore, since all numerical simulations have effective resistivity orders of magnitude higher than the solar value, any viable CME model must predict a negligible dependence of ejection speed on Lundquist number. In order to determine the ejection speed in the simulation, we define the leading edge of the eruption to be the position of the X-point ahead of the plasmoid. This quantity is shown as a function of time in Figure 7. Since B_θ changes sign at the null, we can accurately obtain the position of the X-point by calculating the location of the outermost

extremum in the radial integral of the B_θ flux through the equatorial plane,

$$\int_{r_\odot}^{r} B_\theta(r', \theta, t) r' \sin\theta \; dr'. \tag{16}$$

This procedure has the added advantage that it takes into account the fact that the X-point changes to an O-point late in the evolution.

As the inner flux system expands, the X-point moves outward at a speed determined by the slope of this curve. Just before the plasmoid pinches off due to the onset of flare reconnection, this slope indicates an expansion speed of 50km s^{-1}. Once the flux rope pinches off, at about 73000 seconds, the outer X-point accelerates rapidly, reaching an 'ejection' speed of 365km s^{-1} before it reaches the outer limit of our simulation. Almost all the acceleration occurs below $3r_\odot$. For comparison, the Alfven speed at the equator at 3 solar radii before the flux rope arrives is 65km s^{-1}, and at 45^o north it is 160km s^{-1}, Figure 3. As the plasmoid moves outward, it creates a density enhancement around it as it sweeps up coronal material, Figure 4. Since the plasmoid is moving at supersonic and super-alfvenic speeds, a magnetoacoustic shock forms at the leading edge of this enhancement, Figure 5. These results verify that, at least for this simulation, the breakout model does produce a fast CME.

In order to determine the dependence on resistivity, we have run identical simulations but with refinement levels one lower and one higher than that shown in Figure 2, corresponding to effective grids of 256×512 and 1024×2048 respectively. Grids larger than 1024×2048 are too cpu-intensive to run in reasonable times, and as will be discussed below, 3.2, grids smaller than 256×512 are too inaccurate. The evolution is qualitatively identical for all cases, with a plasmoid ejection as in Figures 1 to 5. For quantitative comparison, Table 1 lists the position and velocity of the outer X-point at approximately 85,000 s when the eruption is fully developed and is approaching its maximum velocity. It is evident that the speed does not decrease with refinement level, in fact, it exhibits a significant increase between the first and second case, and a small increase between the last two cases. We believe the primary reason for this increase is that a larger grid implies a smaller effective resistivity and, consequently, the system can build up more free energy before it begins to reconnect. As is evident from Figure 1, the onset of breakout reconnection and the ejection of the plasmoid occurs well before the end of the shearing phase at, $t = 100,000$ s. Delaying the eruption implies that it will release more free energy and, therefore, have higher initial acceleration. Of course, the maximum velocities in the system are limited by the Alfven speed, and it appears that the last two refinement cases are approaching this limit.

Another important issue for all models is the energetics of the eruption. The fast ejection speed in our simulation implies that the kinetic energy should play a major role. Figure 8

shows the evolution of several important energy terms in the system. Since the system is driven by the shear flow in the azimuthal direction, the bulk of the free energy initially lies in the azimuthal field, B_ϕ^2. The azimuthal energy rises smoothly reaching a maximum at around 65,000 s, and then begins to decrease sharply due to the onset of outward expansion, even though the shearing continues on until 100,000 s. Between 65,000 and 80,000 s, the free energy in the non-azimuthal components, $B_r^2 + B_\theta^2$ rises rapidly, implying that the energy is being transferred from the azimuthal to non-azimuthal components of the field. This time period corresponds to the creation of the radial current sheet deep in the inner flux system, and to the onset of reconnection there. From 80,000 to 90,000 s, the non-azimuthal field decreases sharply, corresponding to a steep rise in kinetic energy. We note that the kinetic energy accounts for approximately half the energy lost by the field, the rest is taken up by the increase in gravitational energy. Since not all the azimuthal field is injected into the plasmoid, a fraction remains in the closed field region that does not erupt, we also show in Figure 8 the azimuthal magnetic energy below 1.5 solar radii. Comparison of the total azimuthal energy with that below 1.5 solar radii, indicates that by the end of the simulation, 120,000 s, almost all the azimuthal magnetic energy in the ejected plasmoid has been lost due to the plasmoid's large expansion.

3.2. Evolution of Helicity

The role of helicity in CMEs has received considerable attention in recent years. Several authors have argued that CMEs are the primary mechanism by which the Sun sheds excess helicity and toroidal flux and, consequently, CMEs may play a key role in the solar cycle (e.g., Bieber & Rust 1995; Kumar & Rust 1996; Low 2001; Rust 2001; Demoulin et al 2002; Nindos et al 2003; Gopalswamy et al 2003). It is important, therefore, to understand the evolution of helicity in models of CME initiation such as breakout. We can investigate this question in detail with our simulations.

Since the Solar surface does not represent a flux surface, the helicity

$$K = \int \boldsymbol{A} \cdot \boldsymbol{B} \; dV \tag{17}$$

is not conserved in ideal MHD. However the relative helicity (Berger & Field 1984; Finn & Antonsen 1985)

$$K_r = \int (\boldsymbol{A} + \boldsymbol{A}_p) \cdot (\boldsymbol{B} - \boldsymbol{B}_p) \; dV \tag{18}$$

is conserved, where $\boldsymbol{B}_p$ is the potential field with the same flux distribution through the surfaces bounding the computational domain as $\boldsymbol{B}$. If we choose $\boldsymbol{B}_p$ to be the initial potential

field given by Equations (5) and (6), then this condition is satisfied, since our line-tying boundary condition at the solar surface requires that B_r not change with time. Under conditions of azimuthal symmetry, the helicity density can be written as (Antiochos et al. 2002)

$$k_r(r, \theta, t) = 2A_\phi B_\phi \tag{19}$$

so the total relative helicity at time t is given by

$$K_r = \int k_r(r, \theta, t)\ dV. \tag{20}$$

In Figure 6 we show the distribution of helicity density at various stages in the evolution of the system. The helicity shed by the ejection of the plasmoid represents approximately 80% of the total originally injected into the system. This result suggests that although CMEs remove the bulk of the coronal helicity, a significant fraction remains behind, which implies that some other mechanism operating in the corona itself must be responsible for dissipating the rest of the helicity. There are several caveats, however, to this conclusion, the main one being that in our simulation we consider only the helicity associated with the neutral line shear. This limits all the helicity carried off by the ejected plasmoid to be contained in an inner core region of the plasmoid comprised of the sheared field. In the real corona there is likely to be considerable helicity associated with large-scale magnetic fields, because of the effects of differential rotation (DeVore 2000) and active region motions on a global scale. If this overlying field opens up during the eruption, then it will lose essentially all its helicity, and the fraction of coronal helicity carried away by a CME could be substantially greater than 80% of the pre-eruption value.

3.2.1. Influence of Spatial Resolution

The helicity density is a useful quantity for investigating not only the physics of the eruption, but also the numerics of the simulation. Since we do not solve an equation for the evolution of helicity density, we can use this quantity as a stringent error measure for the calculation. The rate at which relative helicity is injected into the model at the solar surface is given by the surface integral

$$\frac{dK_r}{dt} = -2 \int B_r A_\phi v_\phi\ dS \tag{21}$$

where dS is an element of the surface.

Based on Taylor's conjecture (Woltjer 1958; Taylor 1974; Berger 1984), we expect the relative helicity to be conserved to a good approximation, because the reconnection caused

by numerical diffusion occurs in only a small fraction of the simulation volume. If we compare the time integral of the helicity injection rate with the volume integrated relative-helicity density, we can check whether this is the case. These quantities are compared in Figure 9, which shows that at the resolution of our calculation, helicity is well conserved even during the strong reconnection and eruption phase. This test is highly sensitive to the spatial resolution. For the same simulation on a grid of 256×512 points we found that helicity was misconserved by 20% and on a grid of 128×256 points by more than 50%. The ultra-high resolution, 1024×2048 run showed an even better agreement between injected and measured helicity than in Figure 9. These results indicate that a grid of 512×1024 is an optimal resolution for the simulation. Larger grids do not add significantly more accuracy, whereas smaller grids start to degrade the calculation noticeably. Figure 9 also demonstrates the robustness and low-diffusivity of our code, and the advantages of using an adaptive mesh for physical systems the the breakout model where we expect current sheets to form in only a few locations.

4. Discussion

We have presented in this paper the first simulations of a complete breakout CME. These calculations have allowed us to answer a number of major questions concerning the eruption. The most important result concerns the speed of the eruption. We find that the model does, indeed, produce fast CMEs with ejection velocities of order the Alfven speed. Even more important, the ejection speed does not appear to be sensitive to the refinement level of the calculation, i.e., to the effective resistivity, at least, for a resistivity with a spatial scale dependence similar to that of numerical resistivity. These two conclusions provide strong support to the breakout model. One caveat, however, is that the simulations presented here are only 2.5D, whereas a real CME is fully 3D. There will clearly be major differences between 3D and 2.5D calculations, in particular, a disconnected flux rope will not form in 3D. But the underlying topology of a multi-polar flux system with null points in the corona remains unchanged in 3D (e.g., Antiochos 1998; Aulanier et al. 2000); therefore, we believe it likely that many of the important results in this paper, such as ejection speed and the general evolution shown in Figures 1 through 5, are likely to remain valid in 3D geometries.

Another important result of the simulations is that although most of the helicity in the system is ejected during eruption, a significant fraction remains in the corona. In fact, this result is to be expected. It is well-known observationally that neutral-line shear does not disappear during an eruptive flare (e.g., Wang et al. 1994). CMEs may responsible for most of the helicity loss of the corona, but it seems clear that some other mechanism, possibly

small-scale diffusion, eliminates the remaining neutral-line shear. This conclusion raises the interesting question as to whether CMEs are essential for eliminating coronal helicity as has been argued by numerous authors.

The work presented here also raises interesting questions concerning observational tests of the breakout model and the implications for CME/eruptive flare prediction. The most convincing observation would be to detect evidence of breakout reconnection before a CME and the accompanying flare. A critical question, therefore, is the amount of breakout reconnection that one would expect to observe before CME and flare onset. The answer can be obtained from Figure 10, which plots the total flux below the outer X-point as a function of time. It is evident that by the end of the simulation, approximately half of the original flux overlying the sheared neutral line has been removed by breakout reconnection. The key point is that most of this reconnection occurs after 80,000 s, i.e., after the rapid acceleration Figure 7 and the flare reconnection, Figure 1, have clearly started. We emphasize, however, that even though the bulk of the breakout reconnection occurs during what would be observed as the eruption/flare, itself, this reconnection is essential for the event to take place. As discussed in Antiochos et al. (1999), the sheared field configuration does not have enough energy to open up the overlying restraining field. This restraining field must be moved out of the way by reconnection.

The implications of our results for observations are that the strongest signatures of breakout are likely to be present during the flare impulsive phase. In retrospect, this finding is not surprising. Breakout reconnection is driven by outward expansion of the field and, hence, will be strongest during the CME rapid acceleration phase when the outward expansion is largest. But a large outward expansion will inevitably produce a current sheet below the erupting flux, which will drive flare reconnection there. In fact, our analysis of the July 14, 1998 eruptive flare showed exactly this behavior (Aulanier et al. 2000). In that event, there was clear evidence of breakout reconnection before flare onset, but the most pronounced signatures were observed during the flare impulsive phase. Our results on the relative timing of breakout reconnection, CME acceleration and flare onset also appear to be in agreement with recent observations by Zhang et al (2001) and Gallagher et al (2003) who find that flare-associated, CMEs have a slowly rising initiation phase, followed by a fast acceleration phase roughly coincident with the flare impulsive phase. With further data analysis and theoretical modeling, especially in 3D, it should be possible to determine whether this CME initiation phase and rapid acceleration are due to magnetic breakout.

This work was supported in part by NASA, NSF, and ONR.

Table 1. X-point Position and Velocity.

Max. Resolution	Radius(units of $r_\odot$)	Velocity(km s^{-1})
256x512	3.6	170
512x1024	4.3	233
1024x2048	4.4	233

Note. — Data refer to time 85000 seconds in each case.

REFERENCES

Aly, J. J. 1984, ApJ, 283, 349

Aly, J. J. 1991, ApJ, 375, L61

Amari, T., Luciani, J. F., Mikić, Z., & Linker, J. 2000, ApJ, 529, L49

Antiochos, S.K. 1998, ApJ, 502, L181

Antiochos, S.K., DeVore, C.R., & Klimchuk, J.A. 1999, ApJ, 510, 485

Antiochos, S.K., Karpen, J.T. & DeVore, C.R. 2002, ApJ, 575, 578

Aulanier, G., DeLuca, E. E., Antiochos, S. K., McMullen, R. A., & Golub, L. 2000, ApJ, 540, 1126

Berger, M. A. & Field, G. B. 1984, J. Fluid Mech., 147, 133

Berger, M. A. 1984, Geophys. and Astrophys. Fluid Dynamics, 30, 79-104

Bieber, J. W. & Rust, D. M. 1995, ApJ, 453, 911

Boris, J. P. 1970, NRL Memorandum Report 2167.

Carmichael, H. 1964, in AAS-NASA Symp. on Physics of Solar Flares, ed. W.N. Ness, (Washington:NASA SP-50), 451

Chen, J. 2001, Space Sci. Rev., 95, 165

Demoulin, P. et al 2002, A&A, 382, 650

DeVore, C.R. 1991, J. of Comput. Phys., 92, 142

DeVore, C.R. 2001, ApJ, 539, 944

Finn, J.M. & Antonsen, T.M. 1985, Comments Plasma Phys. Controlled Fusion, 9, 111

Forbes, T. G. 2000, J. Geophys. Res., 105, 23153

Forbes, T. G., & Isenberg, P. A. 1991, ApJ, 373, 294

Furth, H. P., Killeen, J., & Rosenbluth, M. N. 1963, Phys. Fluids, 6, 459

Gallagher, P. T., Lawrence, G. R., & Dennis, B. R. 2003, ApJ, 588, L53

Gopalswamy, N, Lara, A., Yashiro, S., & Howard, R. A. 2003, ApJ, 598, L63

Hirayama, T. 1974, Sol. Phys., 34, 323

Karpen, J. T., Antiochos, S. K., & DeVore, C. R. 1996, ApJ, 460, L73

Klimchuk, J. A. 2001, in Space Weather, AGU Monograph 125, eds. P. Song, G. Siscoe, & H. Singer (Washington: AGU), 143

Kopp, R.A. & Pneuman, G.W. 1976, Sol. Phys., 50, 85

Kumar, A. & Rust, D. M. 1996, J. Geophys. Res., 101, 15667

Lin, J., Soon, W., & Baliunas, S. L. 2003, New Ast. Rev., 47, 53

Low, B. C., & Smith, D. F. 1993, ApJ, 410, 412

Low, B. C. 1996, Sol. Phys., 167, 217

Low, B. C. 2001, J. Geophys. Res., 106, 25141

Mikić, Z. & Linker, J. A. 1994, ApJ, 430, 898

Moore, R. L., & Roumeliotis, G. 1992, in Eruptive Solar Flares, ed. Svestka, Z., Jackson, B. V., & Machado, M. E. (New York: Springer-Verlag), 69

Nindos, A., Zhang, J., & Zhang, H. 2003, ApJ, 594, 1033

Patty, S. R. & Hagyard, M. J. 1986, Sol. Phys., 103, 111

Priest, E. R., & Forbes, T. 2000, Magnetic Reconnection (Cambridge: University Press)

Rust, D. M. 2001, J. Geophys. Res., 106, 25075

Schmieder, B., Demoulin, P., Aulanier, G., & Golub, L. 1996, ApJ, 467, 881

Sterling, A.C. & Moore, R.L. 2001, ApJ, 560, 1045

Sturrock, P. A. 1966, Nature, 211, 695

Sturrock, P. A. 1989, Sol. Phys., 121, 387

Sturrock, P. A. 1991, ApJ, 380, 655

Taylor, J. B. 1974, Phys. Rev. Lett., 33, 1139

VanBallegooijen, A., & Martens, P. C. H. 1989, ApJ, 343, 971

Wang, H., Ewell, M. W., Jr., Zirin, H., & Ai, G. 1994, ApJ, 424, 436

Wolfson, R., & Saran, S. 1998, ApJ, 499, 496

Woltjer, L. 1958, Proc. Nat. Acad. Sci. USA, 44,489

Wu, S. T., Guo, W. P., & Wang, J. F. 1995, Sol. Phys., 157, 325

Zhang, J., Dere, K. P., Howard, R. A., Kundu, M. R., & White, S. 2001, ApJ, 559, 452

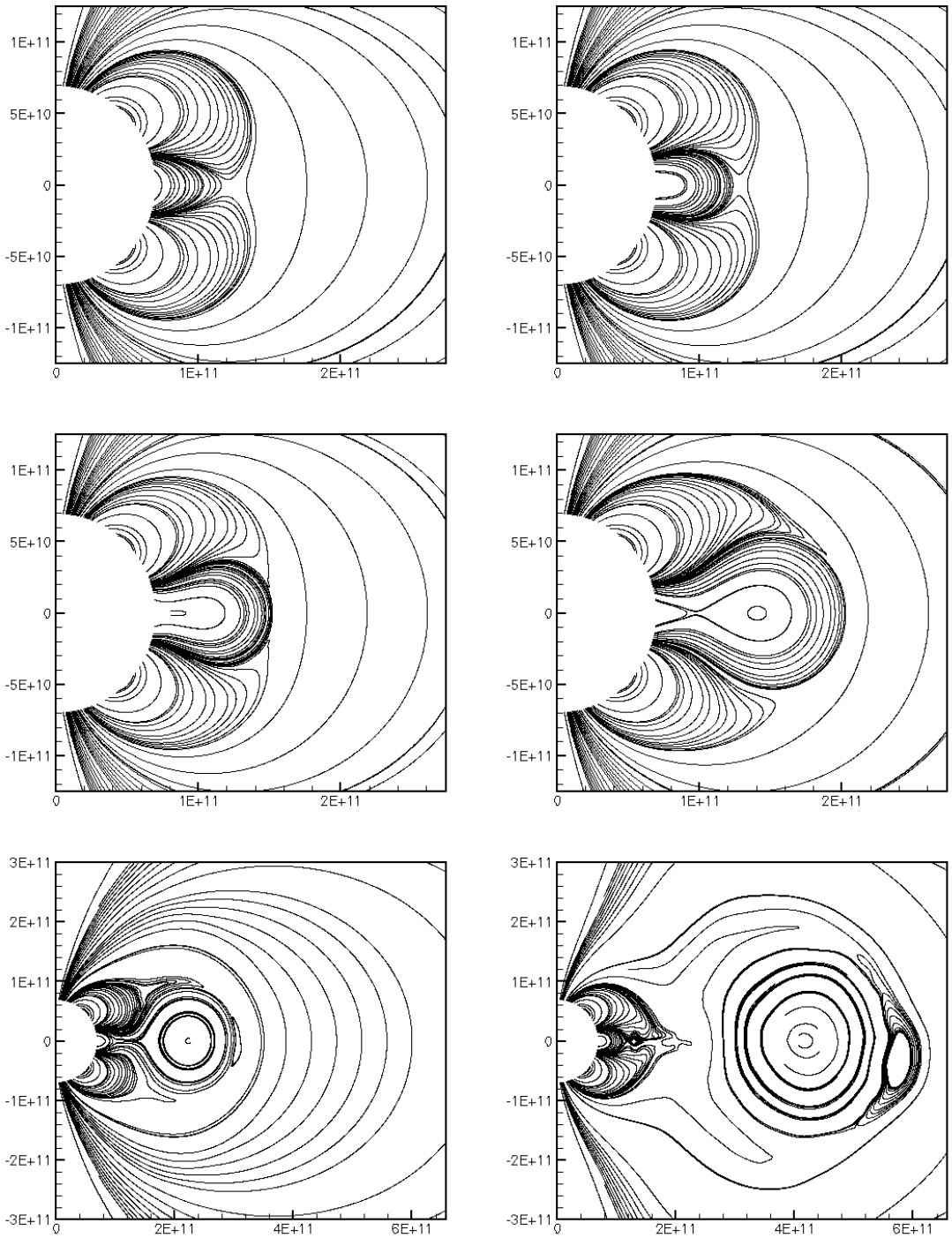

Fig. 1.— Snapshots of selected field-lines in the inner region of the computational domain, projected onto the $\phi = 0$ plane. The times associated with the individual frames are, from left to right and top to bottom, 0, 50251, 70680, 79008, 85185 and 95020 seconds respectively. The spatial scale in the last two frames is expanded to best show the evolving flux rope.

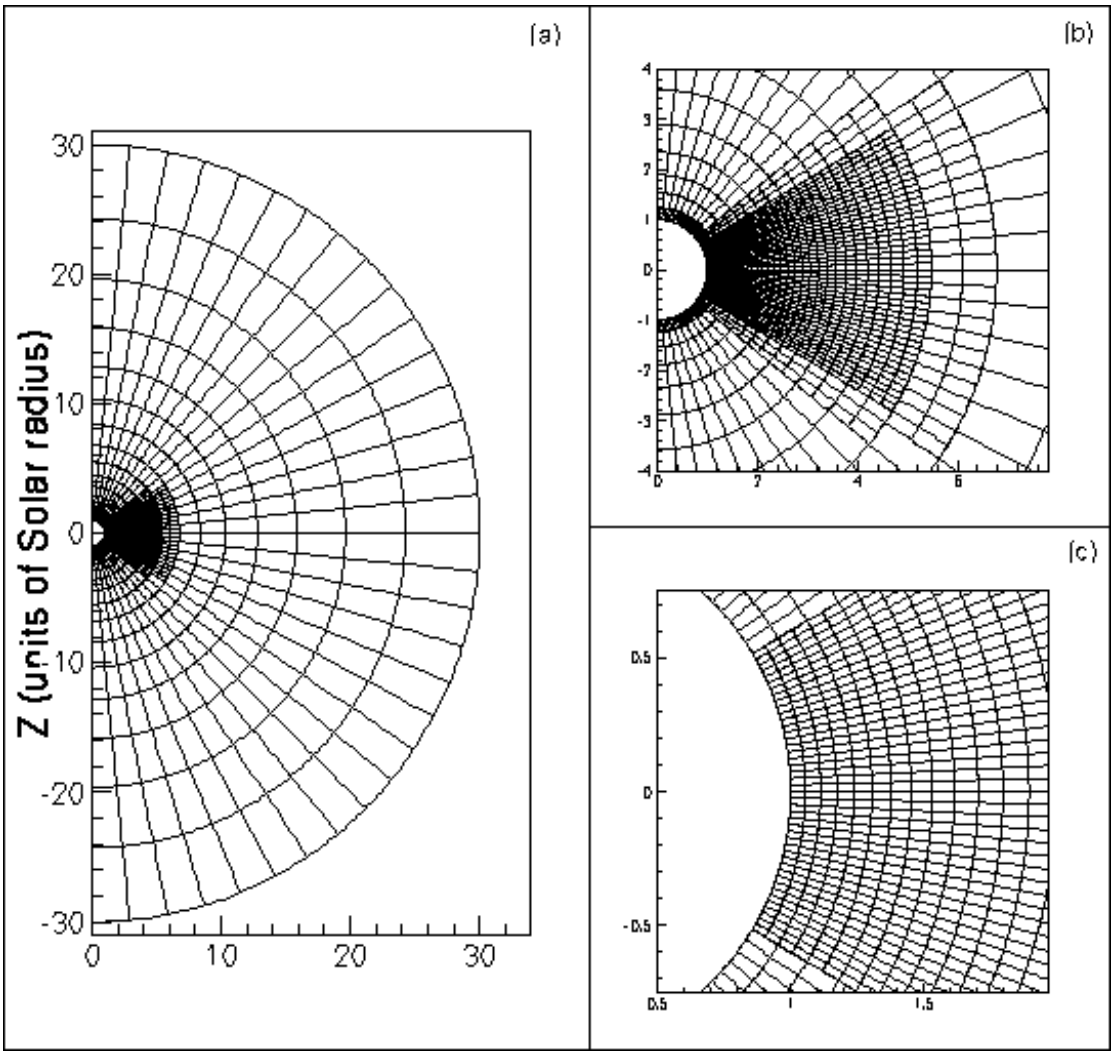

Fig. 2.— The grid used for this computation. Each box represents a block of 8×8 grid cells. Frame (a) is the complete grid, while frames (b) and (c) show successively more enlarged views of the inner equatorial region of the grid.

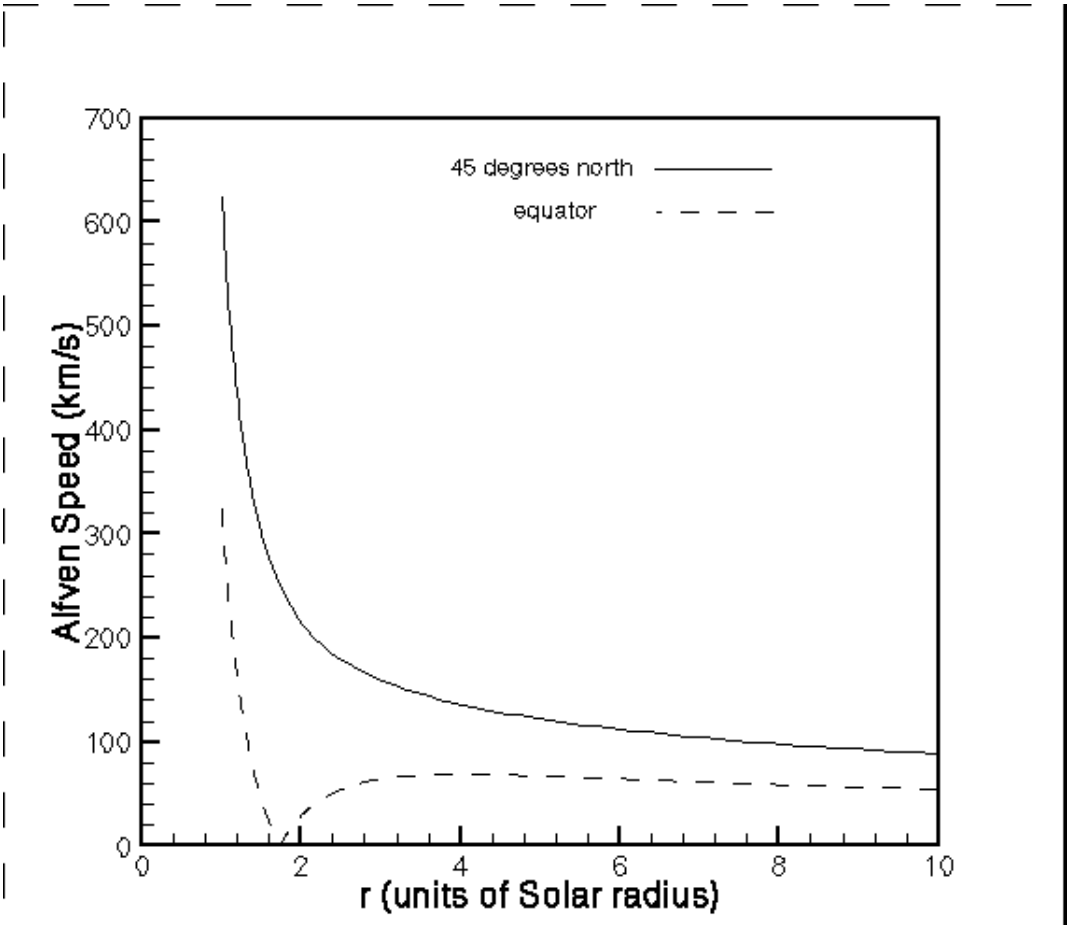
45 degrees north
equator
Alfven Speed (km/s)
r (units of Solar radius)
0
100
200
300
400
500
600
700
0
2
4
6
8
10

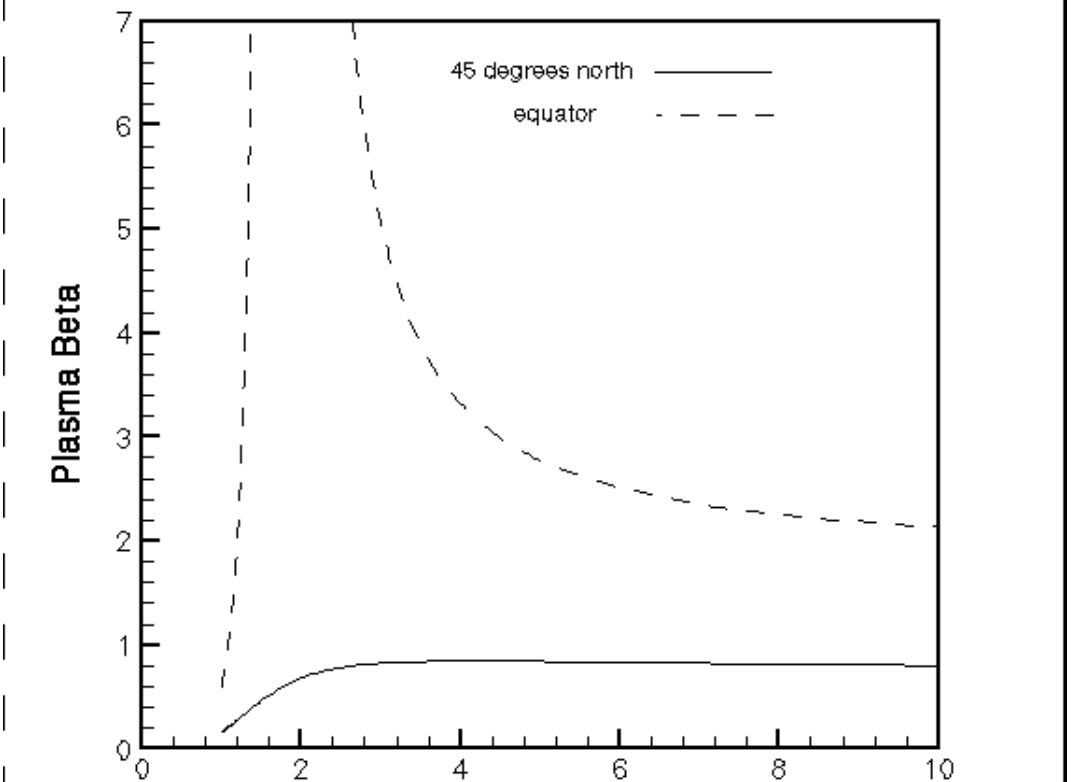
45 degrees north
equator
Plasma Beta
0
1
2
3
4
5
6
7
0
2
4
6
8
10

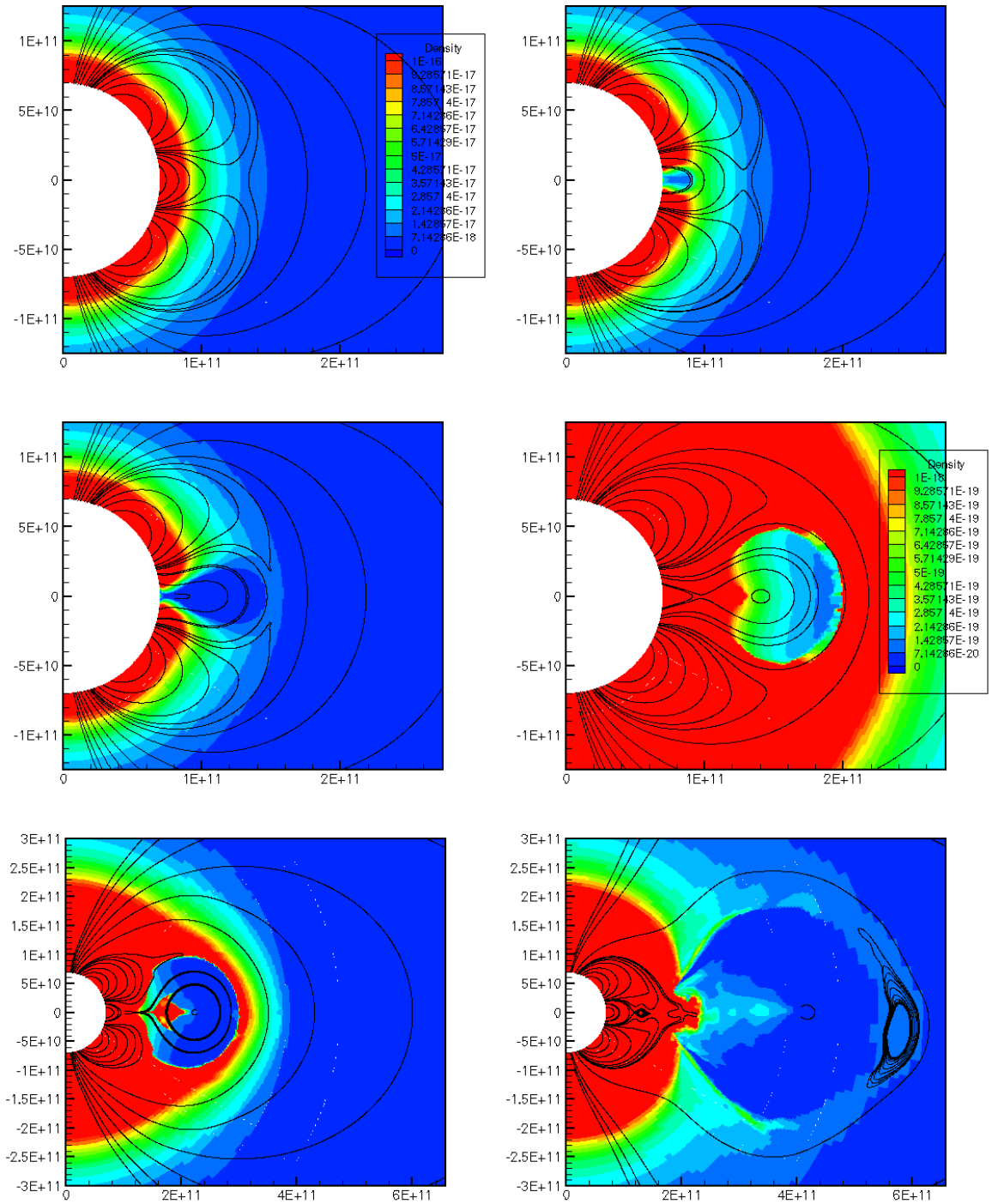

Fig. 4.— Mass density for the frames shown in figure 1. The color map represent mass density in units of gm.cm^{-3}. Some field-lines are superimposed to help compare features in the color map with the corresponding features in the field-line plots. Note, the color map scale is modified in the last three frames to highlight diffuse structure in the expanding flux rope.

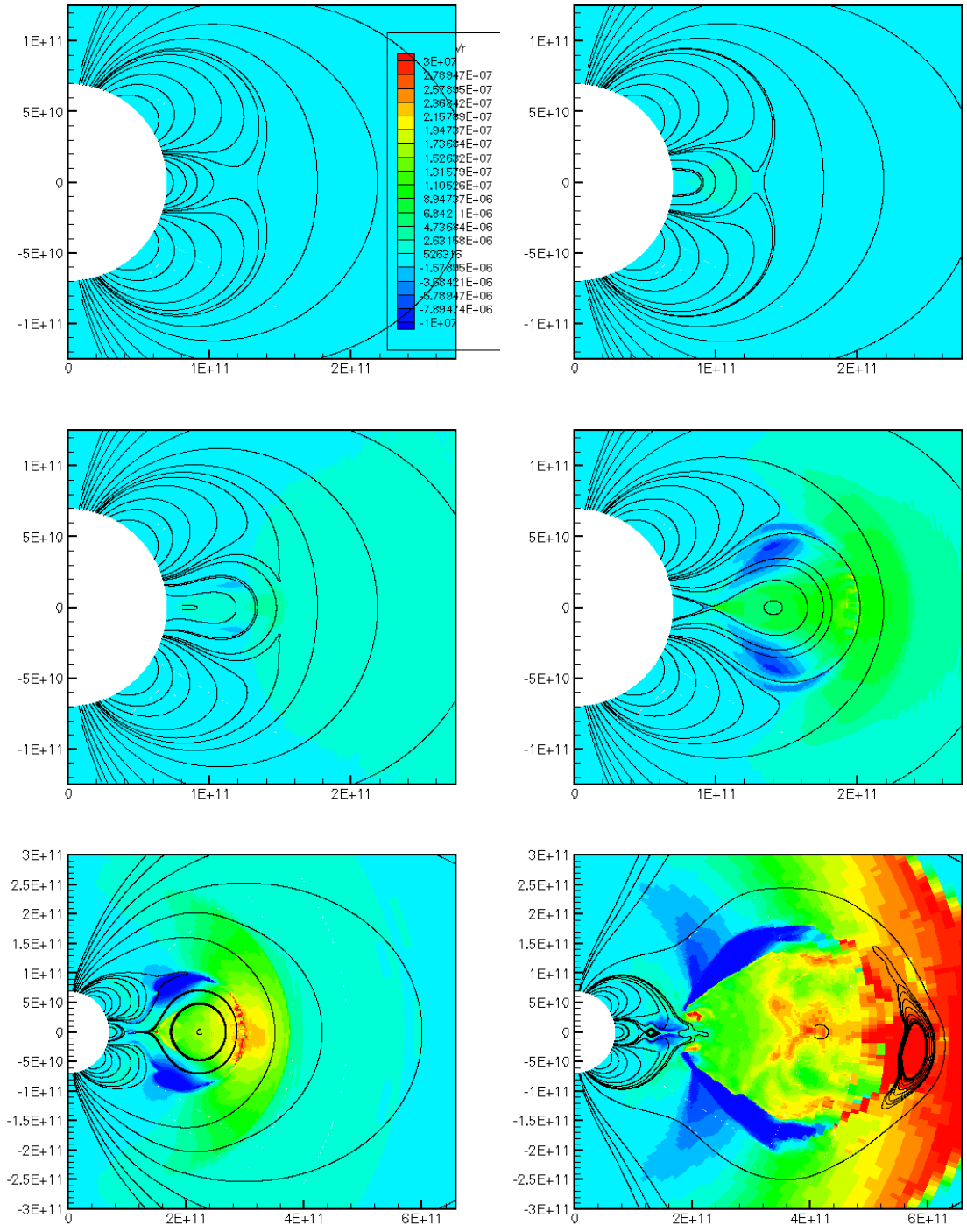

Fig. 5.— Same as figure 4, except the color map represents radial velocity in cm.s^{-1}.

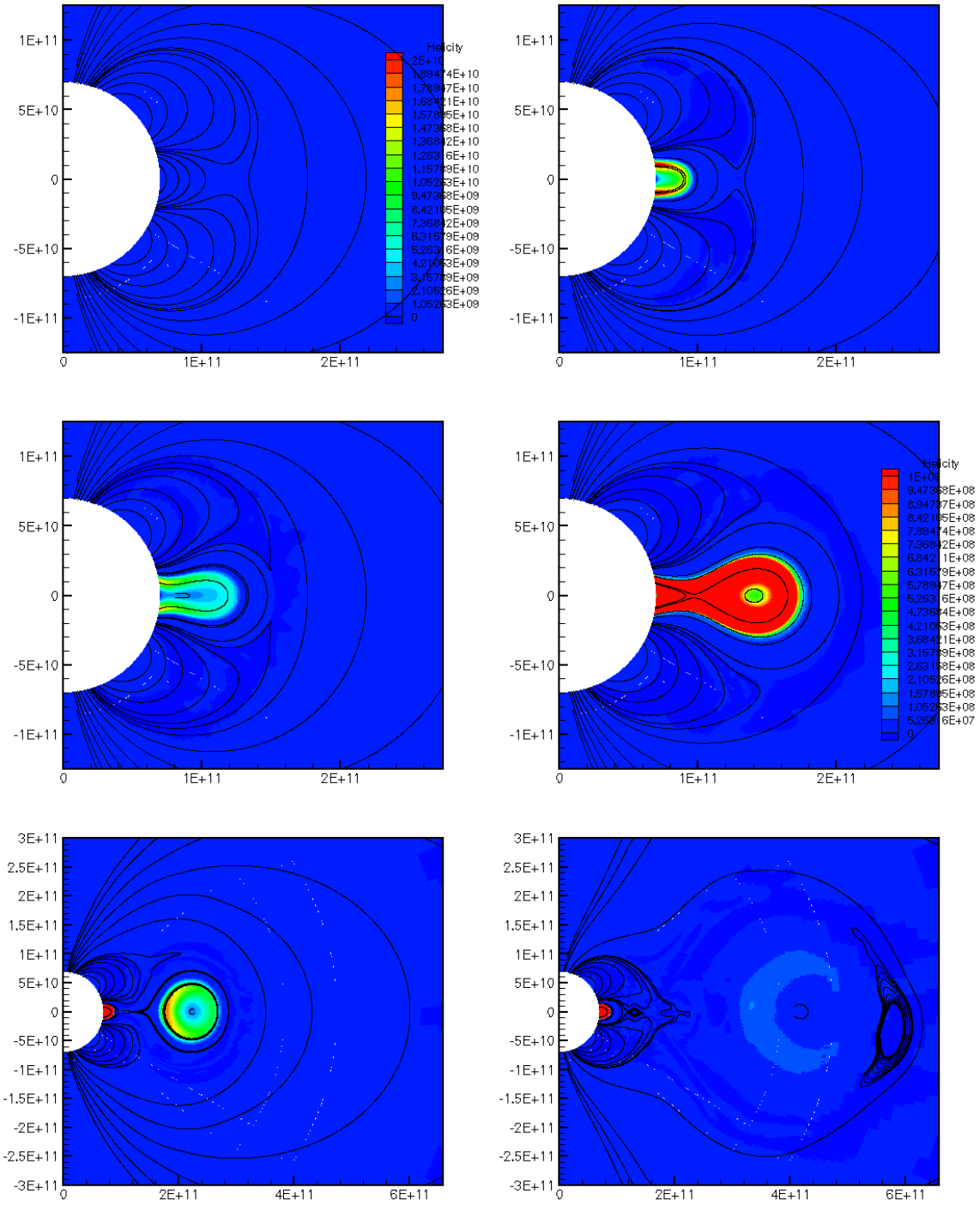

Fig. 6.— Same as figure 4, except the color map represents helicity density. Note, the color map is altered for the last three frames to highlight the lower helicity densities in the expanding flux rope.

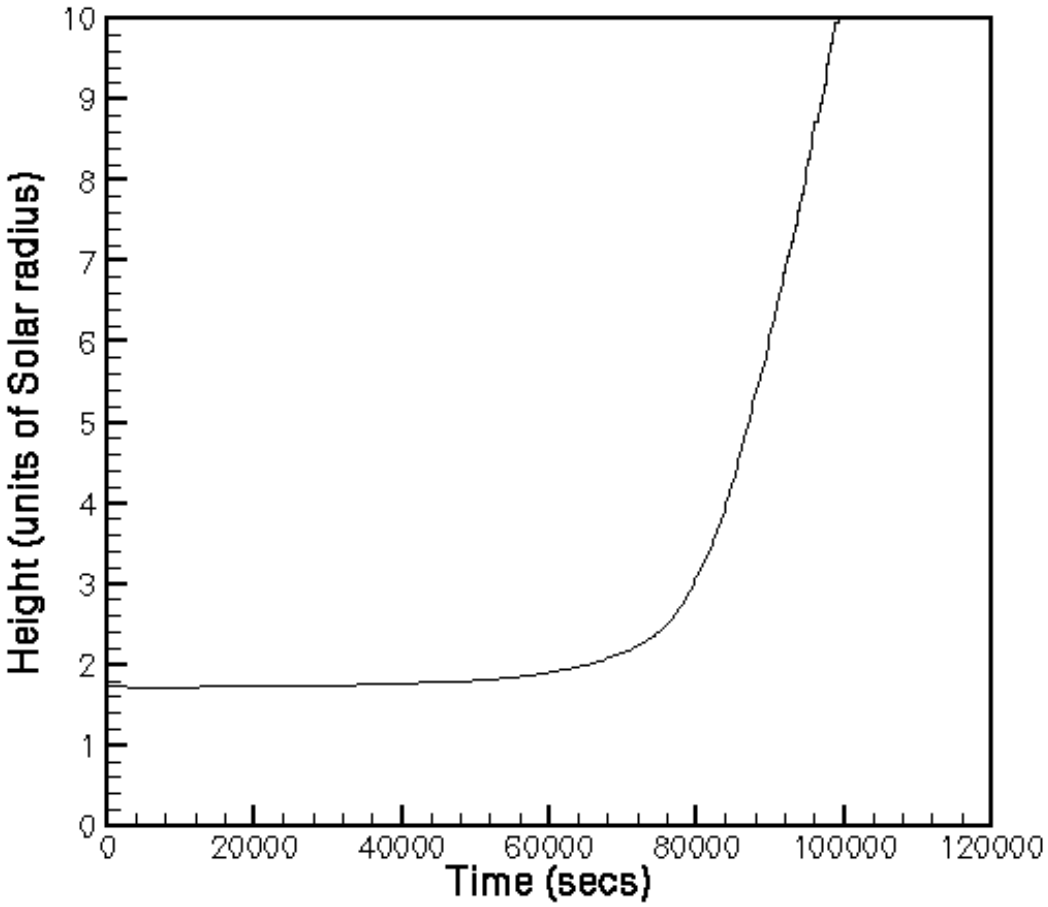

Fig. 7.— This plot tracks the extremum in the radial integral of the flux of B_θ across the equator. It is a proxy for the location of the outer X-point, until the flux rope pinches off, when the curve suddenly jumps to the pinch-off location.

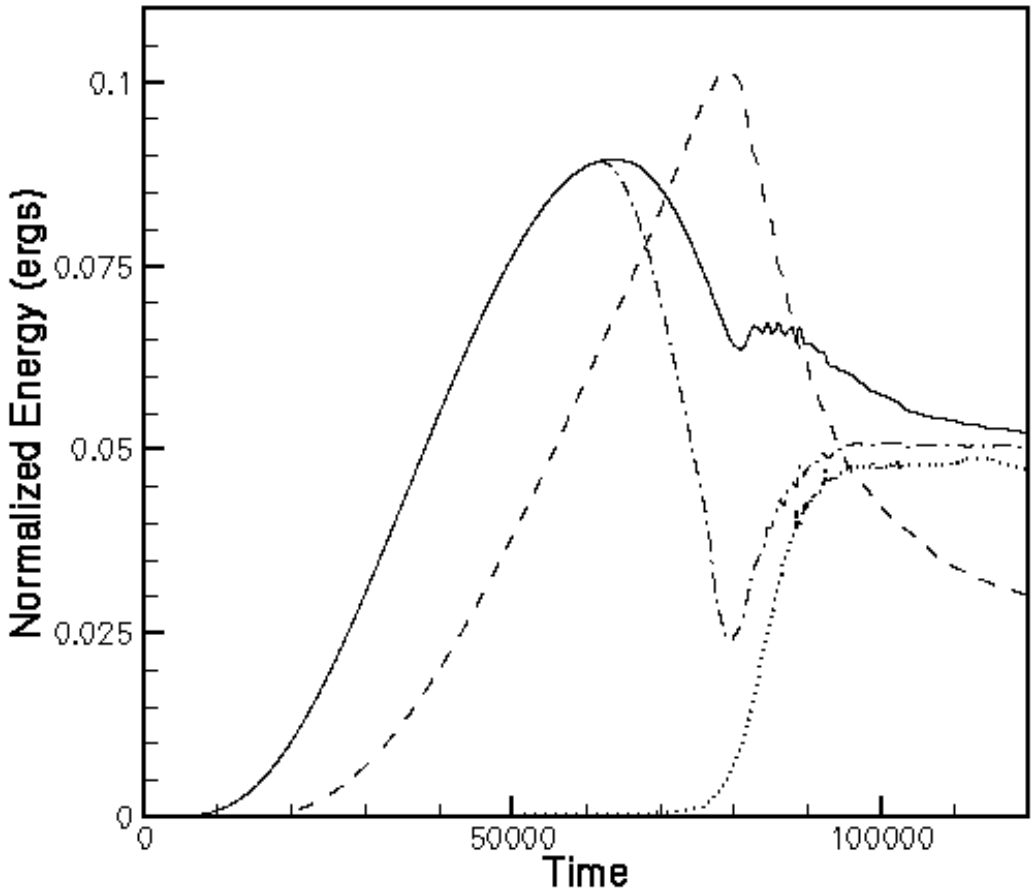

Fig. 8.— Energy components as a function of time. The lines represent azimuthal magnetic energy (solid), the azimuthal magnetic energy below 1.5 solar radii (dash-dot), the change in non-azimuthal magnetic energy from the original field (dash), and the kinetic energy (dotted). The units of energy are ergs divided by the volume $r_{\odot}^3$.

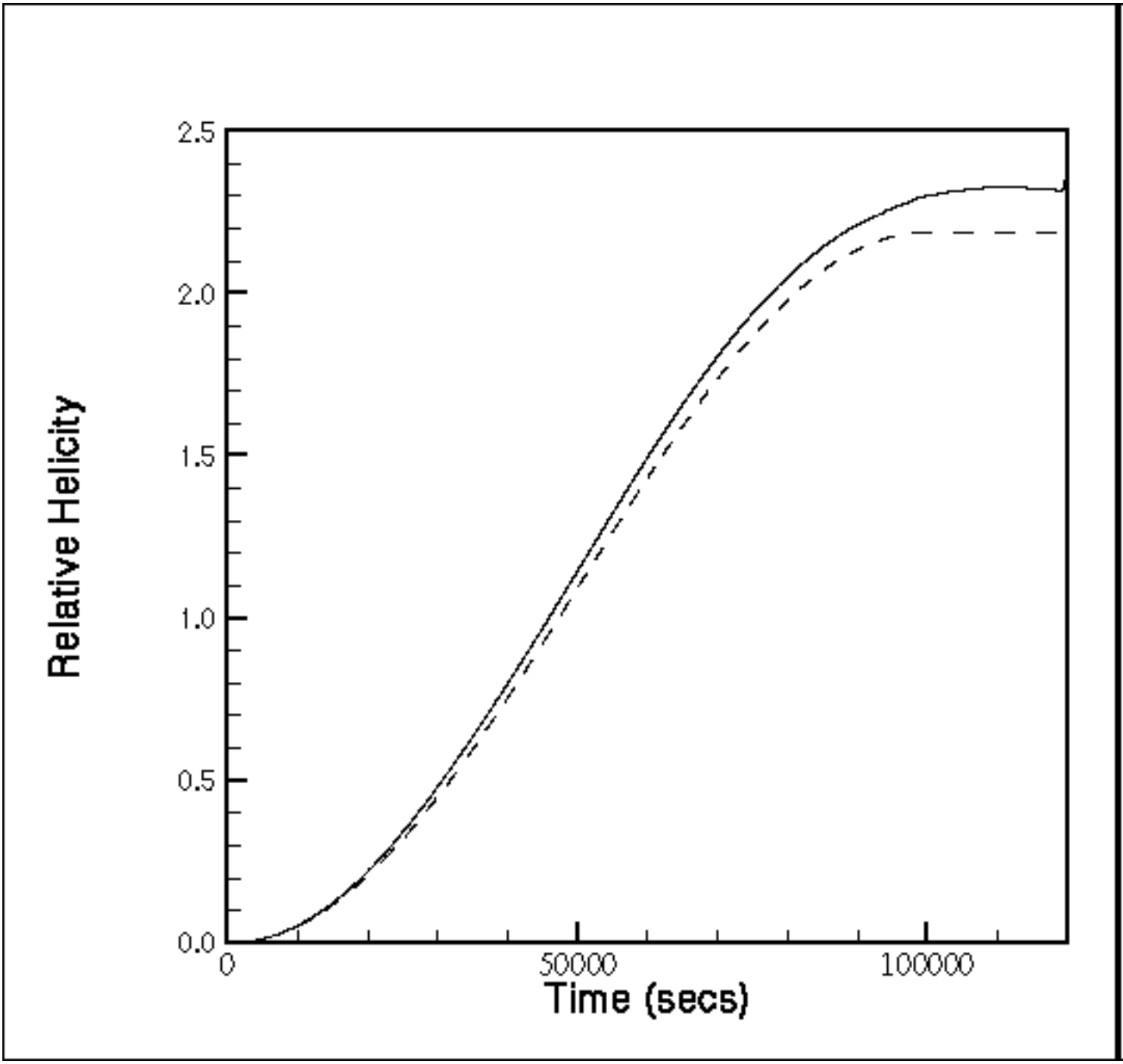

Fig. 9.— Total relative helicity (solid line) in units of $10^{10} r_{\odot}^{3}$ as a function of time, compared with the time integral of the injection rate of relative helicity (dashed line).

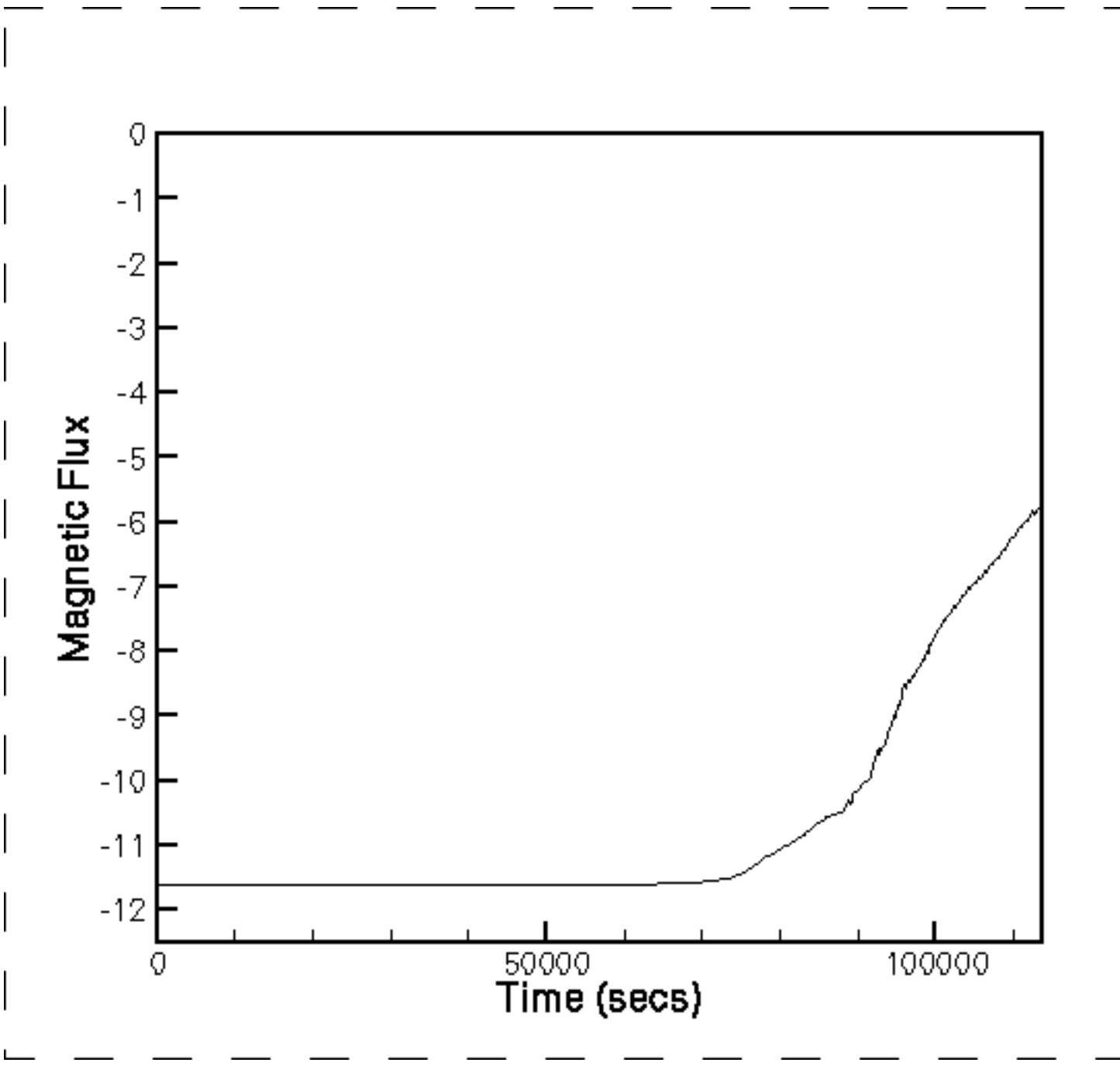

Fig. 10.— The integral of B_θ flux across the equator from the inner boundary to the location of the X-point, plotted as a function of time. The curve is normalized such that -1 is the total B_θ flux across the equator between the inner and outer boundaries.